Philosophical Magazine

ISSN: 1478-6435 (Print) 1478-6443 (Online) Journal homepage: http://www.tandfonline.com/loi/tphm20

Portevin-Le Chatelier effect triggered by complex loading paths in an Al–Cu aluminium alloy

S. C. Ren, T. F. Morgeneyer, M. Mazière, S. Forest & G. Rousselier

To cite this article: S. C. Ren, T. F. Morgeneyer, M. Mazière, S. Forest & G. Rousselier (2018): Portevin-Le Chatelier effect triggered by complex loading paths in an Al–Cu aluminium alloy, Philosophical Magazine, DOI: 10.1080/14786435.2018.1550296

To link to this article: https://doi.org/10.1080/14786435.2018.1550296

Published online: 03 Dec 2018.

PHILOSOPHICAL MAGAZINE
https://doi.org/10.1080/14786435.2018.1550296

Taylor & Francis
Taylor & Francis Group

Portevin-Le Chatelier effect triggered by complex loading paths in an Al–Cu aluminium alloy

S. C. Ren, T. F. Morgeneyer, M. Mazière, S. Forest and G. Rousselier

MINES ParisTech, PSL Research University, Centre des Matériaux, CNRS UMR 7633, BP 87, 91003 Evry, France

ABSTRACT

Serrated flow has been observed during non monotonic tensile tests of an Al–Cu aluminium alloy in the naturally aged state. The associated propagative localisation bands were observed by digital image correlation (DIC). In particular, the Portevin-Le Chatelier (PLC) effect and also Lüders bands were observed in interrupted tests during which the specimen was held for a length of time and also in tests with partial unloading followed by a holding time. Increasing strain rate jumps also triggered the PLC effect. These observations indicate the existence of the PLC effect in this material which was formerly considered insensitive to it at room temperature under monotonic loading conditions. There is no evidence of PLC serrations during constant strain rate tests. A strain ageing finite element model is used that captures the experimentally found PLC triggering effects.

ARTICLE HISTORY
Received 27 March 2018
Accepted 15 November 2018

KEYWORDS
Portevin-Le chatelier effect; AA2139-T3 aluminium alloy; stress relaxation; strain path change; strain rate sensitivity

1. Introduction

The Portevin-Le Chatelier (PLC) effect is revealed by serrated yielding and associated propagation of localisation plastic strain bands at the macroscopic scale. On a microscopic scale, depending on the material, the mechanism is still an issue requiring elucidation due to its complexity. The most commonly accepted explanation is based on the pinning/unpinning of mobile dislocations by diffusion of solute atoms [1], also called dynamic strain ageing (DSA), though other mechanisms, such as pseudo PLC mechanism [2] and precipitate shearing [3], may also be possibilities. Based on the DSA theory, the serrations on the tensile curves and the negative strain rate sensitivity (nSRS) can be adequately explained [4].

In addition to the characterisations of the PLC effect in terms of the nSRS and serrations, the critical strain for PLC instabilities is another important feature. As far as diffusion of solutes is involved, there is a limited active zone of PLC

CONTACT S. Forest samuel.forest@mines-paristech.fr MINES ParisTech, PSL Research University, Centre des Matériaux, CNRS UMR 7633, 87 91003 BP, Evry, France

effect within a certain range of temperature and strain rate. Many experimental observations concerning the onset of PLC instability are based on constant strain rate tensile tests [5,6]. It seems that little emphasis has been made on the influence of interruptions on the triggering of PLC effect [7,8].

However for those studies, the materials (Al-3Mg [7] and FeMcC [8]) are all very sensitive to PLC instabilities in monotonic tensile tests. A recent work [9] reported the occurrence of Lüders effect after strain rate changes with the AA2024 aluminium alloy which, according to the authors, does not show highly serrated flow for monotonic tests. The triggering effect for the PLC effect by relaxation has also been reported for the AA2024 alloy in [10]. However, the 2024 alloy is different from the industrial alloy addressed in the present study. The PLC effect in the AA2024 alloy has been widely reported in the literature even for constant strain rate tests such as in [11]. The tensile test curves of the constant strain rate tests presented in [10] already display slight oscillations.

For an Al–Mg alloy that does show PLC effects during constant strain rate tests, it could be shown that the critical strain to trigger the PLC effect can be influenced by prestraining and ageing [7]. In PLC sensitive FeMnC austenitic steel the critical strain for PLC could be reduced by stress relaxation tests [8].

The current work is also motivated by an earlier work on strain intermittency and the presence of multiple strain localisation bands in the material bulk around the notched area of a compact tension-like specimen made of the material considered in the present study [12]. Strain localisation and intermittent activity have also been found for AA2198-T8R material in [13,14] and 2198-T3R [15] via synchrotron 3D imaging combined with digital volume correlation. The aim of the present study is to gain insight on the origins of the strain intermittency in AA2139-T3. Constant strain rate tests and tests with complex strain rate evolutions have been applied to the material to test its susceptibility to PLC effects.

This may have important consequences for the understanding and improvement of the mechanical properties of such complex industrial alloys used for structural parts. A DSA model implemented in a finite element framework is used to capture the experimental findings.

2. Material and experimental methods

The tested material was taken from a 4.7 mm thick sheet of AA2139 aluminium alloy, in the T3 condition. The production route involved rolling, solution heat treatment, water quenching, cold working by stretching and natural ageing. Copper (4.5–5.5 wt%) was the primary alloying element in this material. Smaller amounts of other elements such as Mg, Mn, Si, Fe, Ag, Ti and Zn were also detected (see Table 1). The exact composition of the alloy can not be provided but it should be close to that provided in [17]. All the samples

Table 1. Chemical composition (wt%) of AA2139 alloy [16].

Cu	Mg	Mn	Si	Fe	Ag	Ti	Zn
4.5–5.5	0.2–0.8	0.2–0.6	≤0.1	≤0.15	0.15–0.6	≤0.15	≤0.25

were cut from AA2139-T3 plates with loading direction along the transverse direction (T). The dimensions of the gauge length area were 4.7 × 6 × 32 mm.

Tests were carried out using a 100 kN MTS machine under displacement control. All the tests were performed at room temperature. Four types of tensile tests were carried out:

(1) Classical monotonic constant strain rate tests with prescribed strain rates of, $10^{-4}s^{-1}$, $10^{-3}s^{-1}$ and $10^{-2}s^{-1}$ (CSR).
   1. Strain rate jump (SRJ) tests : increasing or decreasing strain rate at different strain levels.
   2. Interrupted tests at 2%, 4%, 6%, and 8% strains with 15 seconds of relaxation.
   3. Interrupted tests at 2%, 4%, 6%, and 8% strains with partial unloading and 120 seconds of ageing (UA).

A schematic diagram concerning the displacement evolution applied, as a function of time for those different loading paths is shown in Figure 1. A stereo-DIC system using two Manta G419 cameras (4.1 MPixels each) was synchronised with the tensile machine. The image sampling rate was 20 fps (frames per second) for the CSR and relaxation tests under bulk strain rates $10^{-2}s^{-1}$; 5 fps for the unloading test; 10 fps for $10^{-3}s^{-1}$ CSR; 0.5 fps for $10^{-4}s^{-1}$ CSR; 0.067 fps for $10^{-5}s^{-1}$ CSR. The sampling rates for the strain rate jump tests ranged from 0.1 to 10 fps. The heterogeneous strain measurement on the surface of the tested specimens was performed using VIC-3D software. In the current work, a proper subset size of 25×25 pixels was used to achieve an acceptable measurement error [18]. The calculation step size

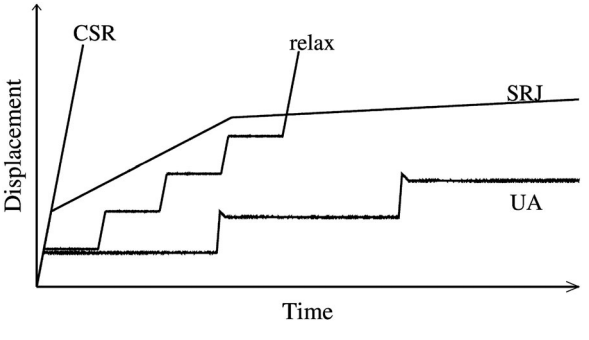

Figure 1. Illustration of displacement evolutions of complex loading tests carried out in this work as function of time: constant strain rate test (CSR), relaxation test (relax), unloading ageing test (UA) and strain rate jump test (SRJ).

was 8 pixels. Using a calibration target, the pixel resolution was determined to be 34 μm/pixel.

3. Experimental results

3.1. Constant strain rate tests

The stress–strain curves of constant strain rate tests are plotted in Figure 2(a). The strain rate sensitivity is characterised by $m = \log(\sigma_i/\sigma_j)/\log(\dot{E}_i/\dot{E}_j)$ [19] where σ_i and σ_j are the stresses measured in tests under bulk strain rates $\dot{E}_i$ and $\dot{E}_j$. Only a very slight negative strain rate sensitivity can be observed at strains from 3% to 12%. All the constant strain rate curves are smooth. PLC related serrations were not observed.

To better illustrate the evolution of PLC bands, a so-called spatio-temporal pattern has been used for describing the location of potential strain bands at different stages in the experiments [20,21]. A Y-line was positioned in the gauge area to measure the incremental axial strain over the whole deformation process. The colour contour was a measure of the ratio between measured strain rate and applied macroscopic strain rate $\dot{\varepsilon}_{yy}/\dot{E}$, where $\dot{\varepsilon}_{yy} \approx \Delta\varepsilon_{yy}/\Delta t$ has been calculated by correlating two successive images with a constant time interval Δt. The maximum ratio was chosen to be 4 as the computed strain rate inside a band was around 5 times the applied strain rate according to DIC measurement. This result is similar to that found in [22].

The spatio-temporal pattern of the constant strain rate tests at a strain rate $10^{-2}s^{-1}$ is shown in Figure 2(b). PLC bands were not observed. The lacking of the PLC effect has also been confirmed in the three other constant strain rate tests.

3.2. Triggering effect found in non-monotonic loading tests

The loading part of the tensile test interrupted by periods of relaxation was conducted at a strain rate of $10^{-2}s^{-1}$. The stress–strain curve of this relaxation test has been superimposed on the corresponding constant strain rate curve at a strain rate $10^{-2}s^{-1}$ in Figure 3(a). Comparing the interrupted test with the constant strain rate curve, the current experimental data show very similar stress levels and ductility. The first stress relaxation was performed at a strain of $= 0.02$. When the specimen was re-loaded after 15 seconds of in-situ ageing by maintaining the cross-head displacement constant, a sharp yield point was found. The following 3 relaxations were performed at strains $= 0.04$,0.06 and 0.08. A static ageing type plateau appeared after each re-loading followed by PLC type serrations.

As shown in Figure 3(b), the strain rate inside a band is greater than 4 times the applied strain rate. Two bands were initiated at opposite ends of the specimen after the second re-straining and propagated to the other side of the gauge area forming an 'X' type pattern over time. This combination of yield peak and

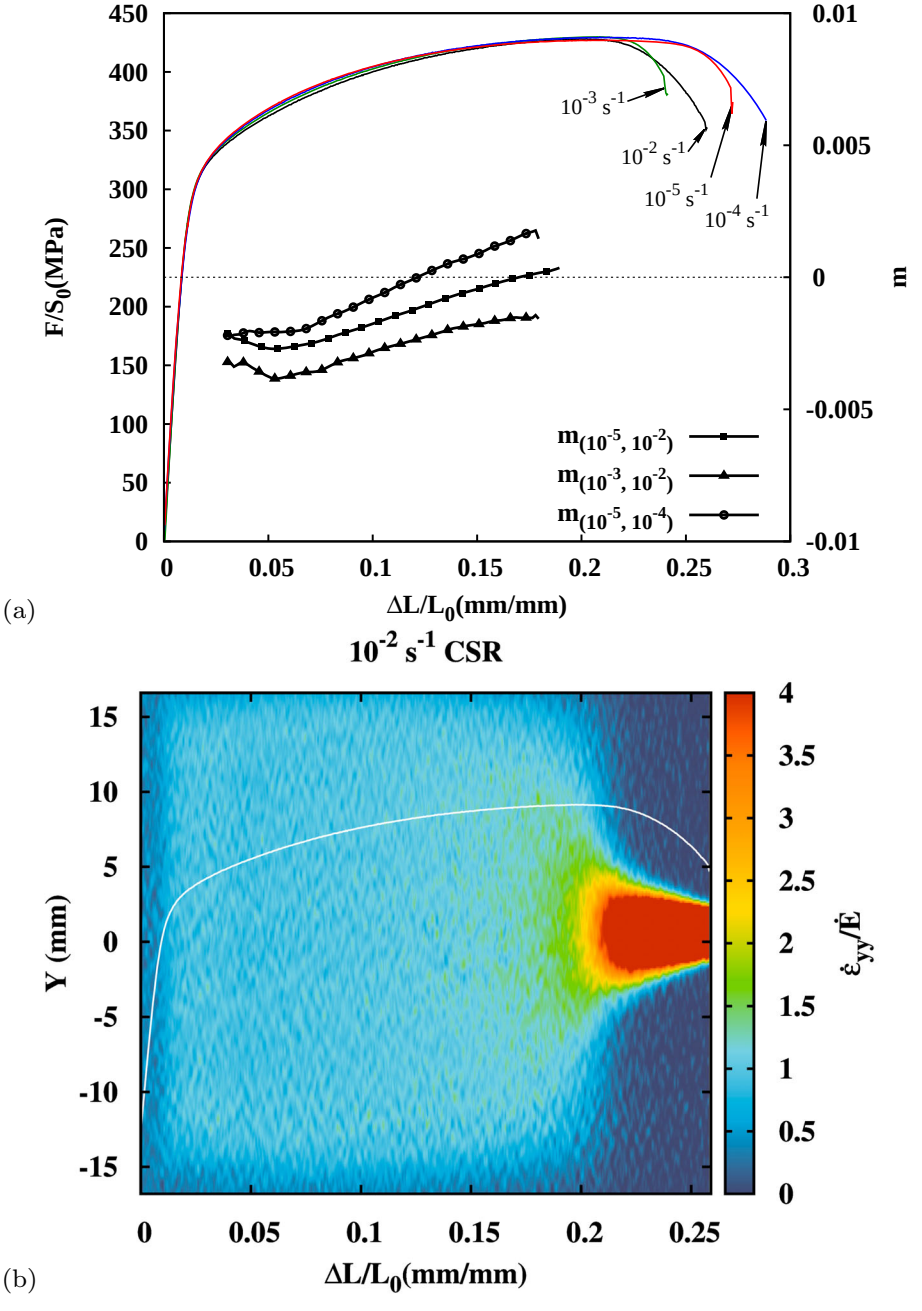

Figure 2. (a) Stress–strain curves for constant strain rate (CSR) tests at different strain rates and the strain rate sensitivity evolution calculated from different strain rate pairs. (b) Experimental spatio-temporal pattern of the CSR test at a strain rate $10^{-2}S^{-1}$ ($\Delta t = 0.2$s).

stress plateau is often observed in aluminium alloys. The first band cannot be distinguished from the following PLC bands. This initial band associated with stress plateau is called a Lüders band. After the third relaxation, a stronger single Lüders band propagated from the upper end to the lower end of the

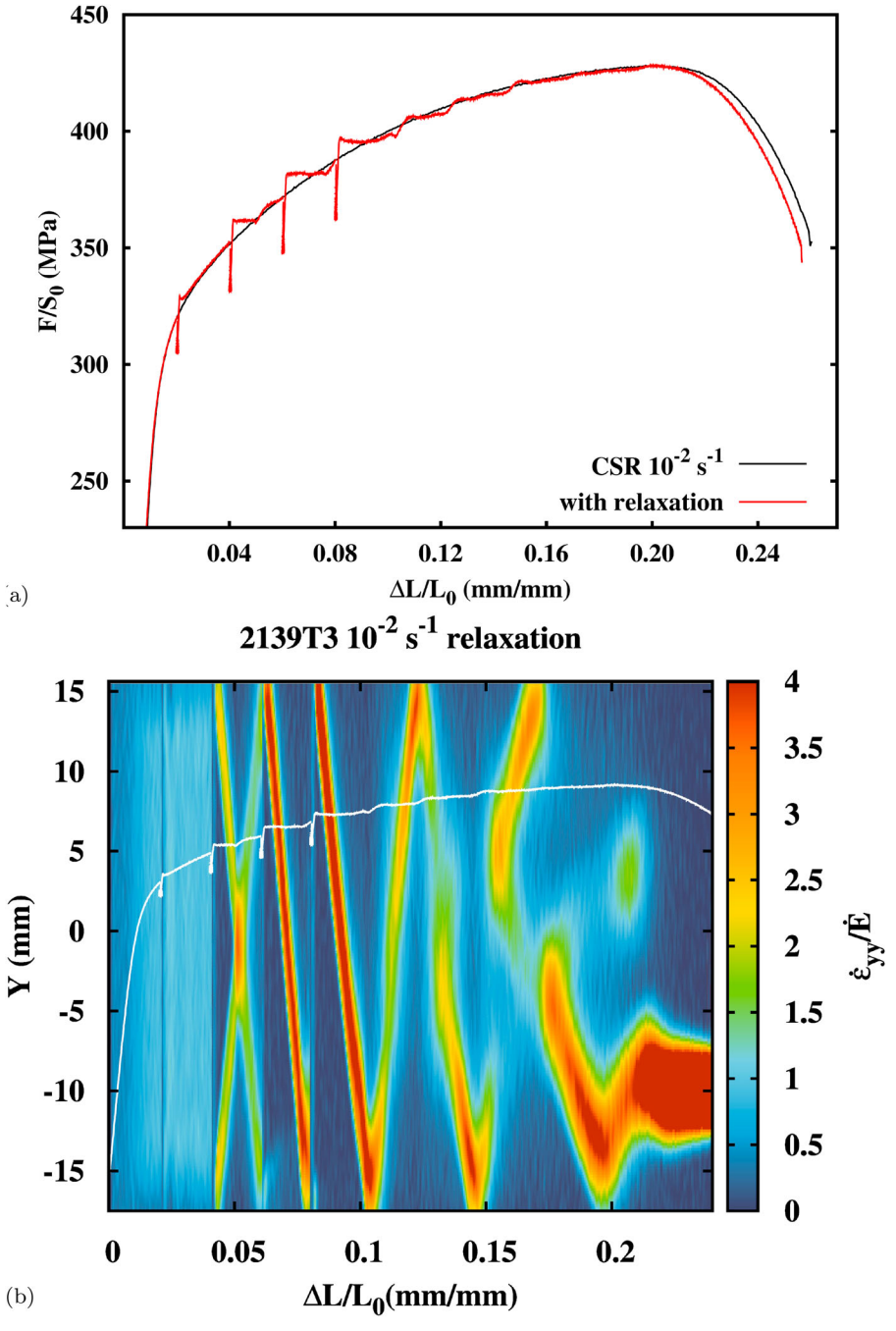

Figure 3. (a) Constant strain rate tensile test at a strain rate $10^{-2}s^{-1}$ (black line) superposed with the curve of tensile test including relaxations. (b) The experimental spatio-temporal pattern of the relaxation test at a strain rate $10^{-2}s^{-1}$ (Δt = 0.05 s).

specimen. During the last stage of deformation, multiple bands appeared. At each instant, two bands with different strengths seem to compete with each other. Finally, a single band became dominant and caused the final fracture.

The corresponding stress–strain curve takes the shape of a staircase. The strain rate field of the gauge area is shown in Figure 3(b) as well as the final fracture image. The bands are horizontal which is due to the section geometry as presented in [21]. A slanted fracture was observed in the thickness plane. A similar fracture mode has also been noticed and discussed by [23]. For a thinner specimen, a slanted band is favoured in the plane across the width.

For the unloading and ageing test (see Figure 4(a)), 4 unloadings were performed at the same strain level as the relaxation test. For each unloading, the stress was maintained for 2 minutes after besing reduced to 14.1 kN (250 MPa). The serrated flow after reloading was very similar to that found during the relaxation test. The spatio-temporal pattern of the unloading test shows very similar localisation (see Figure 4(b)).

Two types of strain rate jump tests, namely the increasing and decreasing strain rate changes, were applied, and are shown in Figure 5. The increasing strain rate curve (start from low strain rate $10^{-5}s^{-1}$) was above the decreasing strain rate curve (start from high strain rate $10^{-2}s^{-1}$) at the beginning part (< 5% strain) and below in the final stage (> 6% strain). This test confirms a slight negative strain rate sensitivity in constant strain rate tests. Each increase in strain rate was accompanied by a yield point, which also indicated that the instantaneous sensitivity was always positive as mentioned in [19,24–26]. It can be noticed that the stress drop of each strain rate jump increased with increasing strain. The steady-state SRS was negative in both of the decreasing and increasing strain rate change tests. The spatio-temporal patterns corresponding to these two strain rate jump tests are illustrated in Figure 5. The pattern is divided into 4 stages corresponding to 4 strain rate states for the increasing test: $10^{-5}s^{-1}$, $10^{-4}s^{-1}$, $10^{-3}s^{-1}$ and $10^{-2}s^{-1}$. At stage III, the serrations have a very low amplitude, however the localisation bands could be seen in DIC measurements. From stage IV onwards, serrations and localisation bands were clearly visible. For the decreasing strain rate jump test, there was neither a sharp yield point nor serrations after reloading. Localisation bands were not observed through DIC measurement either, see Figure 5.

4. Simulation of PLC behaviour

The reloading peak after relaxation or unloading is sometimes called the 'post-relaxation effect' [27,28]. This transient behaviour has been interpreted using the DSA theory and related constitutive models. The solute composition cannot respond to abrupt changes of strain rate [24,29]. The instantaneous SRS was always positive due to the usual thermally activated behaviour. The steady state SRS can be negative or positive. These phenomena have been interpreted based on strain ageing models proposed in literature. However, no effort has been made to investigate the triggering effect. In this part, we will present the simulation results involving relaxation tests using the McCormick type model.

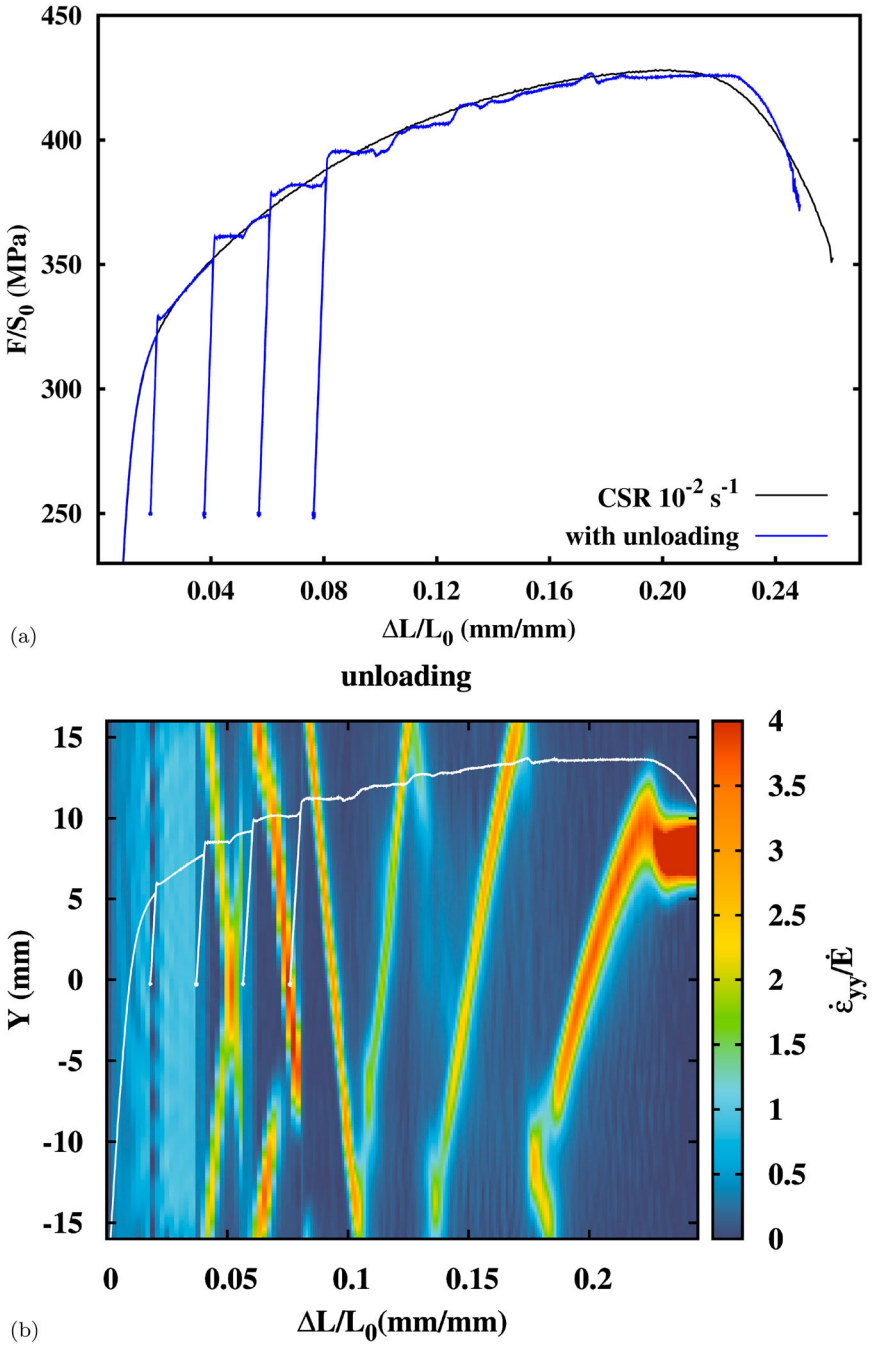

Figure 4. (a) Constant strain rate tensile test at a strain rate $10^{-2}s^{-1}$ (black line) superposed with the curve of tensile test with unloading and ageing (blue curve). (b) The experimental spatio-temporal pattern of the of the tensile test with unloading and ageing at a strain rate $10^{-2}s^{-1}$ (Δt=0.2 s).

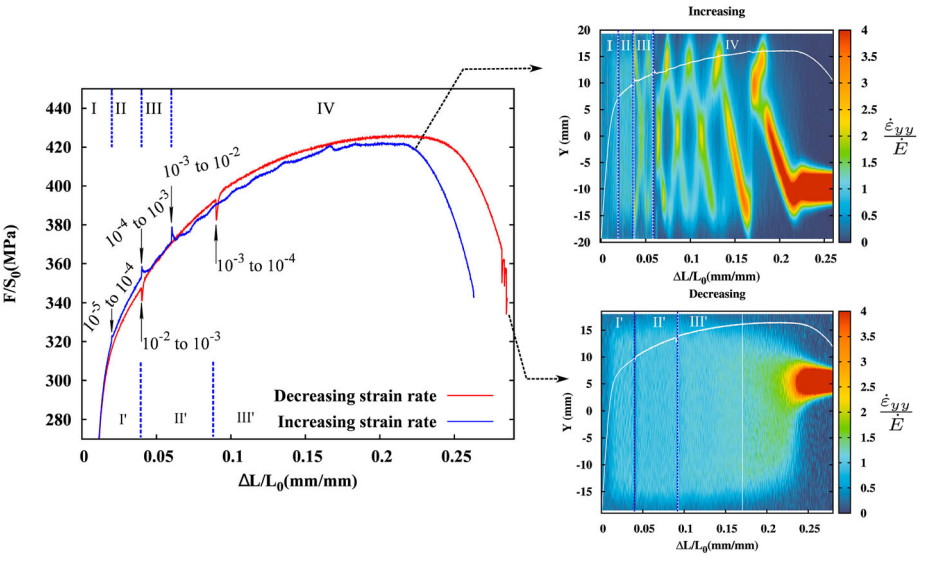

Figure 5. Stress–strain curves of strain rate jump tests: increasing (blue curve) and decreasing (red curve) strain rate jump tests. Right: Experimental spatio-temporal patterns corresponding to these two tests (Δt varies according to strain rate).

4.1. Constitutive equations and identification of the strain ageing model

The McCormick type model [30] has proved to be successful in the modelling and simulation of dynamic strain ageing effects [31–33]. The main equations of the model are

$$f(\underset{\sim}{\boldsymbol{\sigma}}) = \sigma_{eq}(\underset{\sim}{\boldsymbol{\sigma}}) - R(p) - R_a(t_a), \tag{1a}$$

$$R(p) = R_0 + Q_1[1 - e^{-b_1 p}] + Q_2[1 - e^{-b_2 p}], \tag{1b}$$

$$\dot{p} = \dot{\varepsilon}_0 \sinh\left(\frac{\max(0,f)}{\sigma_0}\right). \tag{1c}$$

where f is the yield function, $R(p)$ is one of the conventional hardening functions, and p the cumulated plastic strain.

The ageing hardening term R_a reads

$$R_a(t_a) = P_1 \underbrace{\left[1 - e^{-\left(\frac{t_a}{t_0}\right)^n}\right]}_{C_s}, \quad \dot{t}_a = 1 - \frac{t_a}{w}\dot{p}, \quad t_0 = (1/P_2 p^{\alpha})^{1/n} \tag{2}$$

where P_1 is the magnitude of the maximum stress drop from a fully pinned state to a fully unpinned state; t_0 characterises the time of diffusion process; $n = 0.33$ or 0.66 which corresponds to different diffusion mechanisms; w characterises the strain increment associated with unpinning event.

When the strain rate increases, the solute concentration C_s at dislocations has to decrease with ageing time t_a until reaching the new steady-state controlled by strain rate. A drop in flow stress which follows the initial yield peak occurs in the transient region. When the strain rate decreases, dislocations must wait for a moment before acquiring the new steady state for the lower strain rate. A stress drop is seen after an abrupt strain rate change. With the increase of ageing time, the flow stress is restored and increased.

4.2. Discussion on the spatio-temporal deformation behaviour

4.2.1. Simulation of the triggering effect

Some finite element simulations are performed here using this model for the CSR and relaxation-reloading processes. Parameters are identified based on the current CSR tensile tests (see Table 2). Figure 6 shows the identification result performed on a single integration point together with the experimental curve at a strain rate $\dot{E} = 10^{-2}\text{s}^{-1}$. The 2D and the 3D finite element meshes are shown in Figure 7. The band morphologies simulated on the 2D and the 3D meshes are different. The band reproduced using a 3D mesh is more consistent with experimental observations.

Table 2. Identified parameters for AA2139-T3 alloy.

E(GPa)	v	P_1(MPa)	n	w	$P_2(s^{-n})$	a
69	0.3	33	0.33	5.8×10^{-4}	4.7	0.4
Q_1(MPa)	b_1	Q_2(MPa)	b_2	R_0(MPa)	ε_0	σ_0
64	406	238.5	8.6	225.3	3.5×10^{-6}	3.0

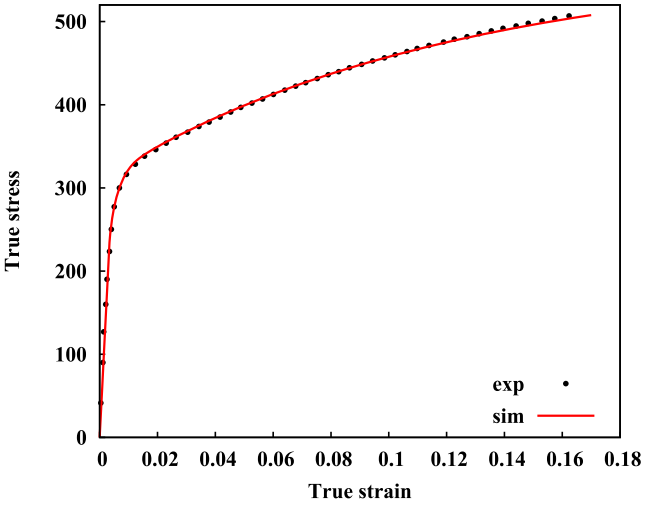

Figure 6. Identification of parameters for AA2139-T3 based on experimental true stress–strain curves.

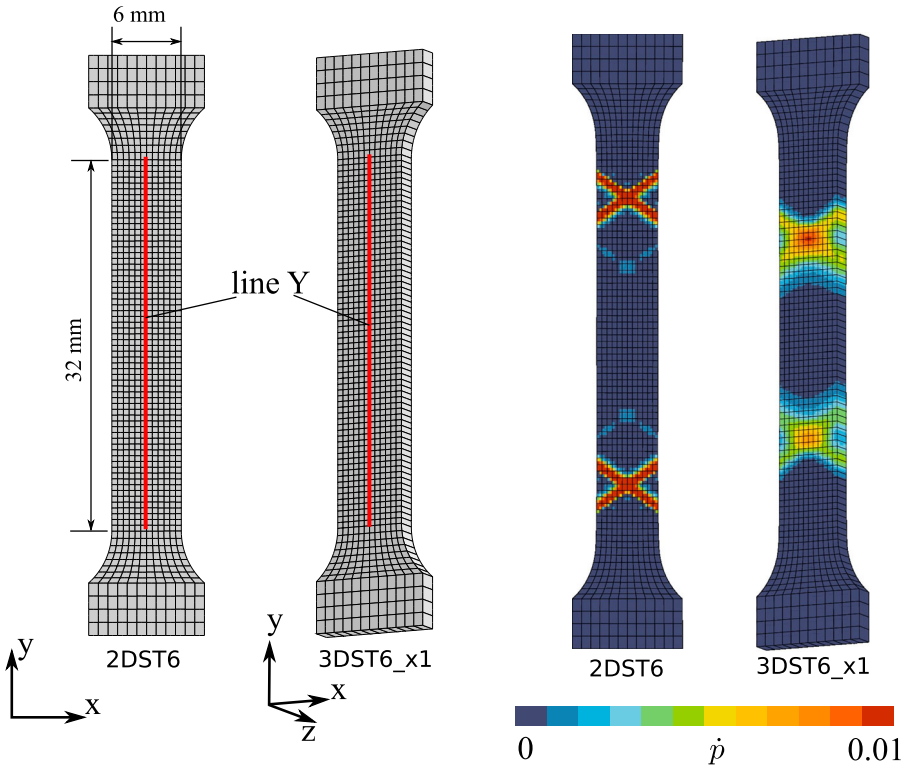

Figure 7. 2D and 3D meshes used for simulations and localisation band after the 4th restraining at $\dot{E} = 10^{-2}s^{-1}$.

Concerning the premature triggering of the critical strain after interruptions, the mechanism is less clear. Balík et al. [7] performed prestrain tests for a binary Al–3Mg alloy in order to test the hypothesis that the initial dislocation density governed the critical strain. Their relaxation and unloading test at room temperature was similar to the results of this study except for a much longer waiting time (>17h), whilst the triggering effect for serrations was very limited. Allain et al. [8] investigated the influence of different relaxation durations and different prestrain levels on the critical strain in an austenitic FeMnC steel. An increasing relaxation period led to the onset of serrations at lower strains. The different prestrain levels did not make any difference to the onset of serrations for their test condition. The authors attributed this effect to the triggering of twinning during relaxation. However, the AA2139 alloy does not present twinning. It is worth noting that the tested austenitic FeMnC steel [8] also shows serrations in a regular tensile test without relaxation at strain states higher than 20%.

In the experiments on the AA2139 alloy, there was no PLC effect observed at room temperature in the investigated strain rate domain 10^{-5}– $10^{-2}s^{-1}$ for constant strain rate tests (CSR), whilst the serrations were triggered after re-straining. To predict such premature triggering effect during relaxation tests, the strain

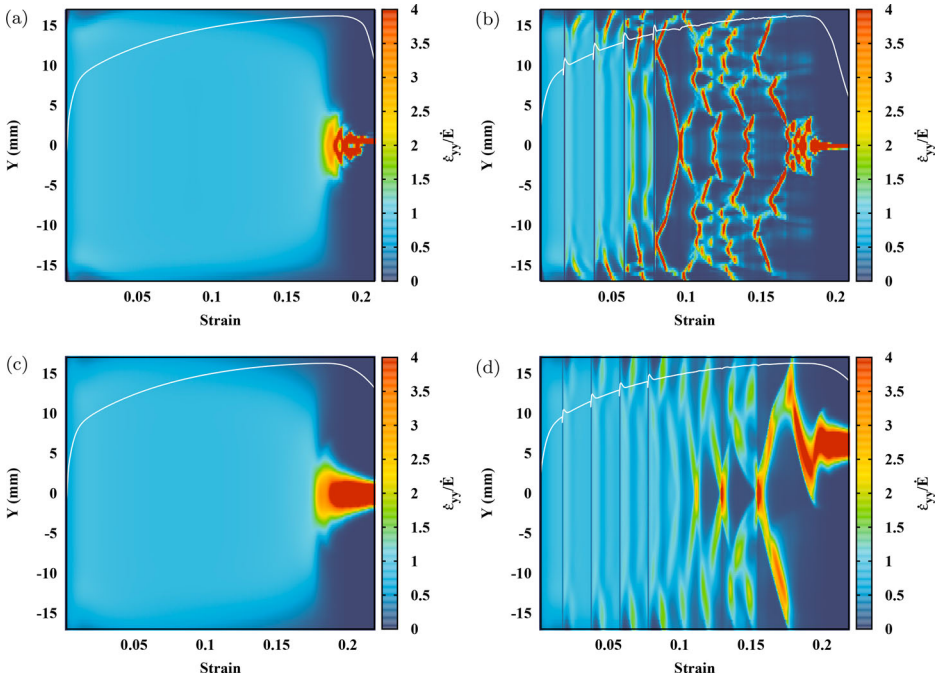

Figure 8. Comparison between numerical spatio-temporal patterns involving 4 relaxations and without relaxation at $\dot{E} = 10^{-2}s^{-1}$. The simulations are performed on 2D (a,b) and 3D (c,d) meshes. (a) CSR at $\dot{E}$=$10^{-2}s^{-1}$ (2D) (b) with 4 relaxations at $\dot{E}$=$10^{-2}s^{-1}$ (2D) (c) CSR at $\dot{E}$=$10^{-2}s^{-1}$ (3D) (d) with 4 relaxations at $\dot{E}$=$10^{-2}s^{-1}$ (3D)

rates $10^{-2}s^{-1}$ and $10^{-3}s^{-1}$ were chosen for finite element simulations. Both simulation results on 2D and 3D meshes at a strain rate of $10^{-2}s^{-1}$ are shown in Figure 8. For the CSR case, the tensile curve is very smooth. Slight serrations and localisation events were found after necking. For the same applied strain rate, when relaxations were involved, serrations appeared much earlier following the 4th re-straining stage (at a strain of = 0.08). Serrations remained visible until final necking. The second and third re-straining also triggered the initiation of slight localisation bands from the two curved transition zones of the specimen as shown in the spatio-temporal pattern. At $\dot{E} = 10^{-2}s^{-1}$, no propagating band could be observed under the constant strain rate condition. At this strain rate, the triggering effect was successfully reproduced after relaxation as well as the lacking of the PLC effect for CSR conditions. It can also be noted that the triggering effect was not influenced by the difference between 2D and 3D meshes. The 3D results are indeed closer to experimental observations in terms of band width and spatio-temporal characteristics.

Very similar to $\dot{E} = 10^{-2}s^{-1}$, the 2D simulation results at $\dot{E} = 10^{-3}s^{-1}$ are shown in Figure 9. The PLC effect was lacking during the CSR simulation but observed after re-straining, although the localisation bands were weaker than for the simulation at $\dot{E}$ =$10^{-2}s^{-1}$.

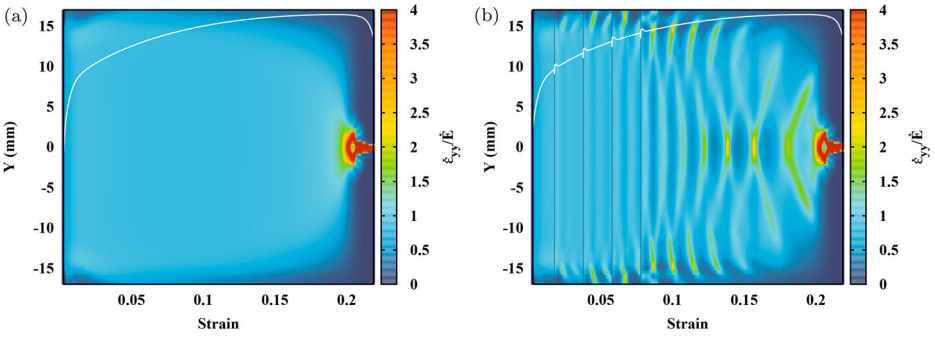

Figure 9. Comparison between numerical spatio-temporal patterns involving 4 relaxations and without relaxation at $10^{-3}s^{-1}$. The simulations are performed on 2D mesh (2DST6). (a) CSR at $\dot{E}=10^{-3}s^{-1}$ (b) with 4 relaxations at $\dot{E}=10^{-3}s^{-1}$

Figure 10 shows the simulation results of strain rate jump tests performed on a 2D mesh (2DST6). The experimentally observed triggering effect during increasing strain rate jump tests has been reproduced successfully with the current parameter set. In accordance with the experimental results shown in Figure 5, the PLC effect was not triggered during the decreasing strain rate jump test. In summary, The FE model with the current parameter set successfully captures the premature triggering of PLC effect observed in this material with good accuracy. This indicates that the McCormick type model used in this work and essentially applied in the literature for monotonic loading

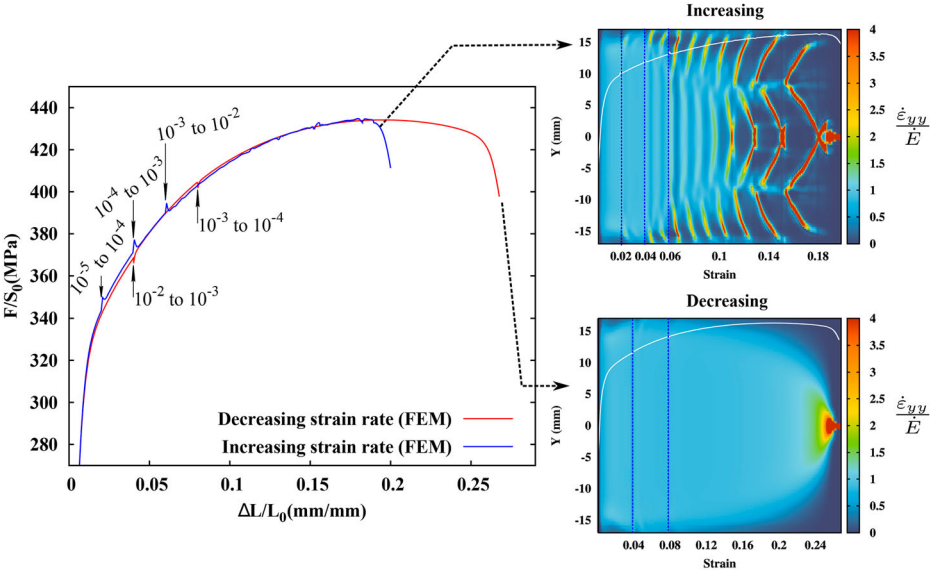

Figure 10. Simulated stress–strain curves of strain rate jump tests: increasing (blue curve) and decreasing (red curve) strain rate jump tests. Right: simulated spatio-temporal patterns using a 2D mesh. This figure can be compared with the experimental results in Figure 5.

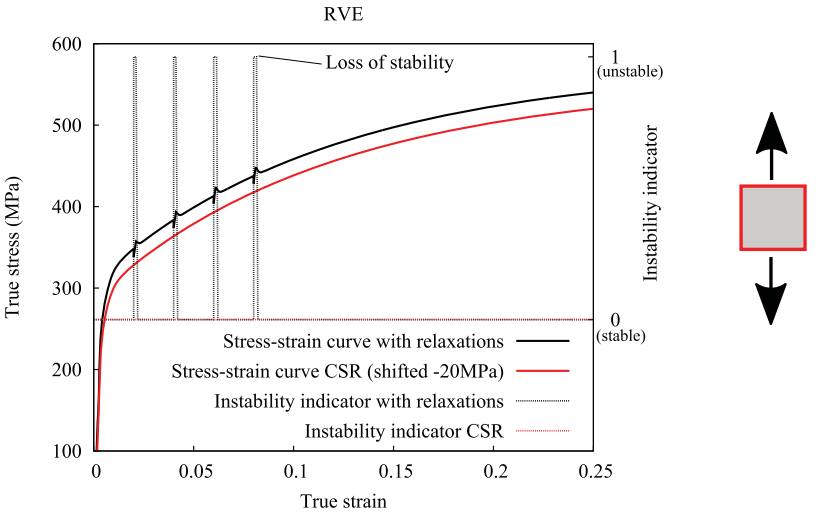

Figure 11. Numerical instability analysis based on a volume element (RVE) performed for both of CSR and relaxation conditions ($\dot{E} = 10^{-2}s^{-1}$).

conditions, contains the main components to predict subtle effects induced by complex loading paths.

4.2.2. Perturbation analysis for studying geometry effects on PLC triggering

In uni-axial tensile tests, the localisation bands were usually found to nucleate at the edge of the curved transition zone to the grip section [34]. To investigate the effect of geometry on the triggering of localisation bands, an instability analysis using the linear perturbation method based on a volume element and full 2D geometry was performed. As presented in [35], the perturbation analysis can be used to predict the critical strain for the onset of PLC effect. Using this method, the influence of relaxation on the prediction of critical strain has been investigated here. In Figure 11, the instability indicator (0 means stable; 1 means unstable) was detected based on a volume element in order to predict the onset of the PLC effect (see [35]). In that case, the relaxations were found to have no influence on the critical strain detected by volume element simulation. The instability indicator jumps from 0 to 1 after reloading and returns quickly to 0. This suggests that the perturbation analysis must be performed for the whole boundary value problem on the sample.

The instability indicator was then computed in the gauge section of the full 2D geometry (see 2DST6 in Figure 7) at all integration points of the mesh. As shown in Figure 12, for the relaxation tests, the indicator reached 1 after the third re-straining oscillating between 0 and 1. After the fourth re-straining, the gauge section lost completely its stability. For CSR condition, the unstable states occurred much later coupled with necking.

After comparing the results obtained for a volume element and for the whole sample, it was concluded that the triggering effect was due to the fact that

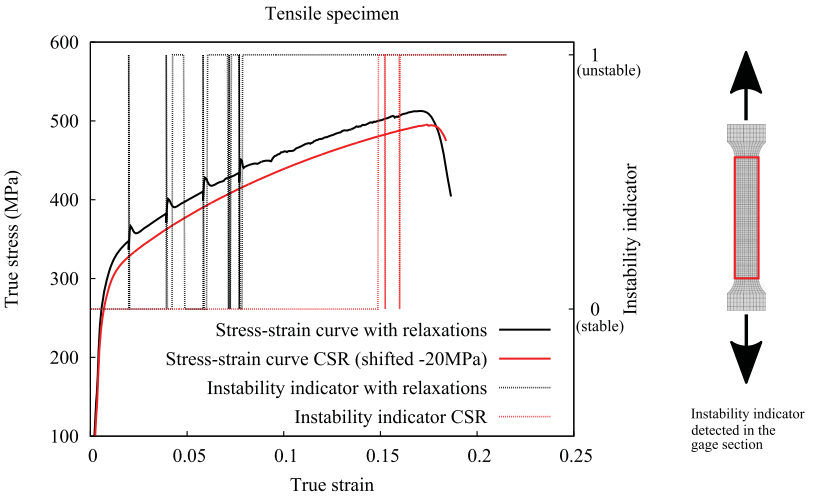

Figure 12. Numerical instability analysis based on a full tensile specimen for both of CSR and relaxation conditions ($\dot{E} = 10^{-2}s^{-1}$). The instability indicator is detected in the gauge section.

instabilities first occur in the curved transition zone before reaching the gauge area. It shows that the strain heterogeneity occurring after re-straining in the curved transition zone was the precursor of Lüders type localisation. The propagation of the Lüders band is thought to be responsible for leaving behind a slightly heterogeneous mechanical state which favours the early triggering of the PLC bands.

4.2.3. Discussion on the effect of alloy elements (Ag) on PLC effect

One of the differences of this alloy composition compared to other 2XXX Al-alloys (i.e. 2024) is the addition of Ag. It could have affected the diffusion properties of the main alloying element Cu and Mg. Some thermo-kinetic simulations were carried out in this work using DICTRA software [36] coupled with the MOBAL3 database to estimate the effect of Ag additions on the diffusion of Cu and Mg in an aluminium based solid solution varying the Ag wt% content between 0 and 0.6 wt%. It was found that the effect of Ag was weak at room temperature and that there could even be a slight increase of the diffusion due to the addition of Ag:

- For Mg, the diffusion coefficient D remained almost unchanged at room temperature and varied from 7.4×10^{-27} to $7.45 \times 10^{-27} m^2 s^{-1}$ when the Ag content was increased from 0 to 0.6 wt.% .
- For Cu, the diffusion coefficient D even increased slightly from 9.8×10^{-30} to $1.9 \times 10^{-29} m^2 s^{-1}$.

It is thus unlikely that the effect of Ag on the diffusion process could have a major impact on the PLC effect. However, there could be an effect of this and other alloying elements on the formation of Cottrell atmospheres. In particular,

the atom radius and the associated molar volume of Ag could promote the formation of Cottrell atmospheres [37]. On the other hand, there was also a chemical effect, which is the driving force for segregation. Ag is soluble in Al [38] like Mg and Cu. Therefore it is very difficult to separate the different effects. A new and demanding study with model materials would be needed to identify the exact contribution of each element to the formation of Cottrell clouds and associated potential PLC effect.

4.3. Perspectives about the triggering effect

The effect found here is of relevance for engineering applications as the forming process might make a material sensitive to the PLC effect. The current standard numerical tools might fail to estimate the real failure event, considering that the presence of the PLC effect could promote the deterioration in mechanical properties, such as a drop of toughness and ductility [39,40]. In addition, Morgeneyer et al. [12], using laminography-DVC measurements, reported the development of early stage strain localisation bands in the notched area of a CT (compact tension) specimen made of AA2139-T3 alloy. They performed stepwise monotonic loading as it is usually done for *insitu* testing procedures. The notch opening displacement was maintained after each load step, thus it can be considered to be a relaxation test. The results of the present work provide a possible explanation for the localisation behaviour observed in [12].

More generally, in any tearing test these phenomena may play a role even for monotonic macroscopic loading as the plastic zone and the fracture process zone are subjected to local strain rate changes due to the stress concentration around the notch and due to crack propagation.

Standard J-δa fracture toughness tests involve partial unloading for the sample compliance measurement and could also trigger PLC effects. Since relaxation and positive strain rate jumps, as shown in the present work, are able to trigger PLC effects, they might be used as standard procedures to test the sensitivity of a material to PLC. In particular, combined with spatio-temporal graphs, a clear picture of the material behaviour can be obtained.

5. Conclusions

The main findings about the anomalous PLC effect in AA2139-T3 alloy are

(1) The PLC effect is not observed in constant strain rate tests at room temperature for the tested strain rates.
(2) The onset of PLC type serrations and localisation is observed in tensile tests with relaxation and unloading ageing.
(3) Comparing the two strain rate jump tests, only the increasing steps triggered PLC instabilities.

(4) The proposed constitutive model captures the experimentally found triggering effect by FE simulations. This is not only true for the triggering effect in the relaxation test (at a strain rate $10^{-2}s^{-1}$) but also for the increasing strain rate test as well as the lacking of PLC during decreasing strain rate test. It seems that the propagation of the Lüders bands following relaxations and increasing strain rates could be responsible for leaving behind a slightly heterogeneous mechanical state which allows the early triggering of the PLC bands.
(5) This alloy contains Ag which is different from other 2xxx alloys. According to thermo-kinetic simulations, there is only a weak effect of Ag addition (0–0.6 wt%) on the diffusion rate. However, it could have an effect on the formation of Cottrell atmospheres.
(6) DIC measurements were found to substantially more reliable for the detection of the PLC effect than the usual analysis of the macroscopic stress–strain curves, as PLC bands were observed with extremely weak serrations.

Acknowledgments

The authors gratefully acknowledge Constellium C-TEC for materials supply. We would like to acknowledge Vladimir A. Esin of the Centre des Matériaux at Mines ParisTech for help with the DICTRA simulations and discussions.

Disclosure statement

No potential conflict of interest was reported by the authors.

Funding

We thank ANR project, with reference ANR-11-BS09-0008, on "Analysis of fracture at low stress for partial funding of this work.

References

[1] A. Cottrell, B. Bilby, *Dislocation theory of yielding and strain ageing of iron*. Proc. Phys. Soc. 62 (1949), pp. 49. http://stacks.iop.org/0370-1298/62/i=1/a=308. Available at http://stacks.iop.org/0370-1298/62/i=1/a=308
[2] Y. Brechet and Y. Estrin, *Pseudo-Portevin-Le Chatelier effect in ordered alloys*, Scripta Mater. 35 (1996), pp. 217–223. Available at http://www.sciencedirect.com/science/article/pii/1359646296001261
[3] F. Chmelík, E. Pink, J. Król, J. Balík, J. Pešička and P. Lukáč, *Mechanisms of serrated flow in aluminium alloys with precipitates investigated by acoustic emission*, Acta Mater. 46 (1998), pp. 4435–4442. Available at http://www.sciencedirect.com/science/article/pii/S1359645498000706
[4] P. Penning, *Mathematics of the Portevin-le Chatelier effect*, Acta Metall. Mater. 20 (1972), pp. 1169–1175. Available at http://www.sciencedirect.com/science/article/pii/0001616072901654

[5] H. Dierke, F. Krawehl, S. Graff, S. Forest, J. Šachl and H. Neuhäuser, *Portevin-Le Chatelier effect in Al-Mg alloys: Influence of obstacles - experiments and modelling*, Comp. Mater. Sci. 39 (2007), pp. 106–112. Available at http://www.sciencedirect.com/science/article/pii/S092702560600139X

[6] S. Fu, T. Cheng, Q. Zhang, Q. Hu and P. Cao, *Two mechanisms for the normal and inverse behaviors of the critical strain for the Portevin–Le Chatelier effect*, Acta Mater. 60 (2012), pp. 6650–6656. Available at http://www.sciencedirect.com/science/article/pii/S1359645412005745

[7] J. Balík, P. Lukáč and L. Kubin, *Inverse critical strains for jerky flow in Al-Mg alloys*, Scripta Mater. 42 (2000), pp. 465–471. Available at http://www.sciencedirect.com/science/article/pii/S1359646299003735

[8] S. Allain, O. Bouaziz, T. Lebedkina and M. Lebyodkin, *Relationship between relaxation mechanisms and strain aging in an austenitic femnc steel*, Scripta Mater. 64 (2011), pp. 741–744. Available at http://www.sciencedirect.com/science/article/pii/S1359646210008699

[9] S. Gupta, A. Beaudoin and J. Chevy, *Strain rate jump induced negative strain rate sensitivity (NSRS) in aluminum alloy 2024: Experiments and constitutive modeling*, Mat. Sci. Eng. A 683 (2017), pp. 143–152. Available at http://www.sciencedirect.com/science/article/pii/S0921509316314927

[10] A. Leacock, R. McMurray, D. Brown, K. Poston, E. Cueto and F. Chinesta, *The influence of strain rate variations on the appearance of serrated yielding in 2024-T3 Al-clad aluminium alloy*, in *AIP Conference Proceedings*, Vol. 907. AIP, 2007, pp. 390–395, Available at http://aip.scitation.org/doi/abs/10.1063/1.2729545

[11] T. Böhlke, G. Bondár, Y. Estrin and M. Lebyodkin, *Geometrically non-linear modeling of the Portevin-Le Chatelier effect*, Comp. Mater. Sci. 44 (2009), pp. 1076–1088. Available at http://www.sciencedirect.com/science/article/pii/S0927025608003601

[12] T. Morgeneyer, T. Taillandier-Thomas, A. Buljac, L. Helfen and F. Hild, *On strain and damage interactions during tearing: 3D in situ measurements and simulations for a ductile alloy (AA2139-T3)*, J. Mech. Phys. Solids 96 (2016), pp. 550–571. Available at http://www.sciencedirect.com/science/article/pii/S0022509615301861

[13] T. Morgeneyer, T. Taillandier-Thomas, L. Helfen, T. Baumbach, I. Sinclair, S. Roux and F. Hild, *In situ 3D observation of early strain localisation during failure of thin Al alloy (2198) sheet*, Acta Mater. 69 (2014), pp. 78–91. Available at http://www.sciencedirect.com/science/article/pii/S1359645414000500

[14] A. Buljac, T. Taillandier-Thomas, T. Morgeneyer, L. Helfen, S. Roux and F. Hild, *Slant strain band development during flat to slant crack transition in AA2198 T8 sheet: In situ 3D measurements*, Int. J. Fracture 200 (2016), pp. 49–62. Available at http://dx.doi.org/10.1007/s10704-015-0052-z

[15] A. Buljac, L. Helfen, F. Hild and T. Morgeneyer, *On deformation and damage micromechanisms in strong work hardening 2198 T3 aluminium alloy*, Acta Mater. 149 (2018), pp. 29–45.

[16] T.F. Morgeneyer, J. Besson, H. Proudhon, M. Starink and I. Sinclair, *Experimental and numerical analysis of toughness anisotropy in AA2139 Al-alloy sheet*, Acta Mater. 57 (2009), pp. 3902–3915. Available at http://www.sciencedirect.com/science/article/pii/S135964540900278X

[17] U. Prisco, A. Squillace, A. Astarita and C. Velotti, *Influence of welding parameters and post-weld aging on tensile properties and fracture location of AA2139-T351 friction-stir-welded joints*, Materials Research 16 (2013), pp. 1106–1112.

[18] X. Xu, Y. Su, Y. Cai, T. Cheng and Q. Zhang, *Effects of various shape functions and subset size in local deformation measurements using dic*, Exp. Mech. 55 (2015), pp. 1575–1590. Available at http://dx.doi.org/10.1007/s11340-015-0054-9

[19] R. Picu, G. Vincze, F. Ozturk, J. Gracio, F. Barlat and A. Maniatty, *Strain rate sensitivity of the commercial aluminum alloy AA5182-O*, Mat. Sci. Eng. A 390 (2005), pp. 334–343. Available at http://www.sciencedirect.com/science/article/pii/S0921509304010652

[20] F. Chmelík, A. Ziegenbein, H. Neuhäuser and P. Lukáč, *Investigating the Portevin-Le Châtelier effect by the acoustic emission and laser extensometry techniques*, Mat. Sci. Eng. A 324 (2002), pp. 200–207. Available at http://www.sciencedirect.com/science/article/pii/S0921509301013120

[21] R. Nogueira de Codes and A. Benallal, *Influence of specimen geometry on the Portevin-Le Châtelier effect due to dynamic strain aging for the AA5083-H116 aluminum alloy*, J. Mech. Mater. Struct. 6 (2011), pp. 951–968. Available at 10.2140/jomms.2011.6.951

[22] Y. Cai, Q. Zhang, S. Yang, S. Fu and Y. Wang, *Experimental study on three-dimensional deformation field of Portevin–Le Chatelier effect using digital image correlation*, Exp. Mech. 56 (2016), pp. 1243–1255. Available at http://dx.doi.org/10.1007/s11340-016-0138-1

[23] Y. Cai, S. Yang, Y. Wang, S. Fu and Q. Zhang, *Characterization of the deformation behaviors associated with the serrated flow of a 5456 Al-based alloy using two orthogonal digital image correlation systems*, Mat. Sci. Eng. A 664 (2016), pp. 155–164. Available at http://www.sciencedirect.com/science/article/pii/S0921509316303641

[24] P. McCormick, *Theory of flow localisation due to dynamic strain ageing*, Acta Metall. Mater. 36 (1988), pp. 3061–3067. Available at http://www.sciencedirect.com/science/article/pii/0001616088900430

[25] C. Ling and P. McCormick, *Strain rate sensitivity and transient behaviour in an Al-Mg-Si alloy*, Acta Metall. Mater. 38 (1990), pp. 2631–2635. Available at http://www.sciencedirect.com/science/article/pii/095671519090275L

[26] C. Ling and P. McCormick, *The effect of temperature on strain rate sensitivity in an Al-Mg-Si alloy*, Acta Metall. Mater. 41 (1993), pp. 3127–3131. Available at http://www.sciencedirect.com/science/article/pii/095671519390042Q

[27] Z. Drozd, Z. Trojanová and S. Kúdela, *Deformation behaviour of Mg-Li-Al alloys*, J. Alloy Compd. 378 (2004), pp. 192–195. Available at http://www.sciencedirect.com/science/article/pii/S0925838804001525

[28] Z. Trojanová, Z. Drozd, P. Lukáč and F. Chmelík, *Deformation behaviour of Mg–Li alloys at elevated temperatures*, Mat. Sci. Eng. A 410 (2005), pp. 148–151. Available at http://www.sciencedirect.com/science/article/pii/S0921509305008580

[29] S.H. van den Brink, A. van den Beukel and P.G. McCormick, *Strain rate sensitivity and the Portevin-Le Chatelier effect in Au-Cu alloys*, Phys. Status Solidi A 30 (1975), pp. 469–477. Available at http://dx.doi.org/10.1002/pssa.2210300205

[30] S. Zhang, P. McCormick and Y. Estrin, *The morphology of Portevin–Le Chatelier bands : Finite element simulation for Al–Mg–Si*, Acta. Mater. 49 (2001), pp. 1087–1094.

[31] S. Graff, S. Forest, J.L. Strudel, C. Prioul, P. Pilvin and J.L. Béchade, *Strain localization phenomena associated with static and dynamic strain ageing in notched specimens: Experiments and finite element simulations*, Mater. Sci. Eng. A 387–389 (2004), pp. 181–185.

[32] S. Graff, S. Forest, J.L. Strudel, C. Prioul, P. Pilvin and J.L. Béchade, *Finite element simulations of dynamic strain ageing effects at V–notches and crack tips*, Scr. Mater. 52 (2005), pp. 1181–1186.

[33] M. Mazière, J. Besson, S. Forest, B. Tanguy, H. Chalons and F. Vogel, *Numerical aspects in the finite element simulation of the Portevin-Le Chatelier effect*, Comput. Method. Appl. M. 199 (2010), pp. 734–754. Available at http://www.sciencedirect.com/science/article/pii/S004578250900379X

[34] B. Klusemann, G. Fischer, T. Böhlke and B. Svendsen, *Thermomechanical characterization of Portevin–Le Châtelier bands in AlMg3 (AA5754) and modeling based on a modified Estrin–McCormick approach*, Int. J. Plasticity 67 (2015), pp. 192–216. Available at http://www.sciencedirect.com/science/article/pii/S074964191400206X

[35] M. Mazière and H. Dierke, *Investigations on the Portevin-Le Chatelier critical strain in an aluminum alloy*, Comp. Mater. Sci. 52 (2012), pp. 68–72. Available at http://www.sciencedirect.com/science/article/pii/S0927025611003120

[36] J.O. Andersson, T. Helander, L. Höglund, P. Shi and B. Sundman, *Thermo-calc & dictra, computational tools for materials science*, Calphad 26 (2002), pp. 273–312. Available at http://www.sciencedirect.com/science/article/pii/S0364591602000378

[37] Y. Mishin and J.W. Cahn, *Thermodynamics of cottrell atmospheres tested by atomistic simulations*, Acta Mater. 117 (2016), pp. 197–206. Available at http://www.sciencedirect.com/science/article/pii/S1359645416305092

[38] T.B. Massalski, J. Murray, L. Bennett and H. Baker, *Binary alloy phase diagrams. vol. i and ii*, Am. Soc. Metals (1986), pp. 2224.

[39] E. Amar and A. Pineau, *Interpretation of ductile fracture toughness temperature dependence of a low strength steel in terms of a local approach*, Eng. Fract. Mech. 22 (1985), pp. 1061–1071. Available at http://www.sciencedirect.com/science/article/pii/001379448590044X

[40] H. Wang, C. Berdin, M. Mazière, S. Forest, C. Prioul, A. Parrot and P. Le-Delliou, *Experimental and numerical study of dynamic strain ageing and its relation to ductile fracture of a C-Mn steel*, Mat. Sci. Eng. A 547 (2012), pp. 19–31. Available at http://www.sciencedirect.com/science/article/pii/S092150931200439X